ELSEVIER

Available online at www.sciencedirect.com

SCIENCE DIRECT®

International Journal of Solids and Structures 42 (2005) 4258–4277

INTERNATIONAL JOURNAL OF SOLIDS and STRUCTURES

www.elsevier.com/locate/ijsolstr

An elasto-plastic model for granular materials with microstructural consideration

C.S. Chang [a,*], P.-Y. Hicher [b]

[a] *Department of Civil and Environmental Engineering, University of Massachusetts, 30 Marston Hall, Amherst, MA 01002, USA*
[b] *Research Institute in Civil and Mechanical Engineering, UMR CNRS 6183, Ecole Centrale Nantes-University of Nantes, France*

Received 17 February 2004; received in revised form 15 September 2004

Abstract

In this paper, we have extended the granular mechanics approach to derive an elasto-plastic stress–strain relationship. The deformation of a representative volume of the material is generated by mobilizing particle contacts in all orientations. Thus, the stress–strain relationship can be derived as an average of the mobilization behavior of these local contact planes. The local behavior is assumed to follow a Hertz–Mindlin's elastic law and a Mohr–Coulomb's plastic law. Essential features such as continuous displacement field, inter-particle stiffness, and fabric tensor are discussed. The predictions of the derived stress–strain model are compared to experimental results for sand under both drained and undrained triaxial loading conditions. The comparisons demonstrate the ability of this model to reproduce accurately the overall mechanical behavior of granular media and to account for the influence of key parameters such as void ratio and mean stress. A part of this paper is devoted to the study of anisotropic specimens loaded in different directions, which shows the model capability of considering the influence of inherent anisotropy on the stress–strain response under a drained triaxial loading condition.

Keywords: Granular material; Stress–strain relationship; Packing anisotropy; Elastic–plastic model

1. Introduction

Microstructural models for elastic stress–strain behavior of granular material can be derived from properties of inter-particle contacts. Considering the mean behavior of all contacts in each orientation,

* Corresponding author. Tel.: +1 413 545 5401; fax: +1 413 545 4525.
E-mail address: chang@ecs.umass.edu (C.S. Chang).

0020-7683/$ - see front matter © 2004 Elsevier Ltd. All rights reserved.
doi:10.1016/j.ijsolstr.2004.09.021

the overall stress strain behavior can be obtained as an average of the contact behavior for all orientations. Models based on this approach can be found in the work by Jenkins (1988), Wallton (1987), Rothenburg and Selvadurai (1981), Chang (1988), Emeriault and Cambou (1996), Liao et al. (2000), Kruyt and Rothenburg (2002), among others.

As for microstructural models for more complex elasto-plastic behavior of granular material, the approach is not as straightforward as that used in elastic models. We can generally classify them into two categories. The first category is *plasticity models with fabric tensor*, in which the material parameters of plasticity are defined at the macro (particle assembly) level. A fabric tensor is utilized to represent the anisotropy of packing structure (see Satake, 1997) and material parameters are made to be functions of the fabric tensor so that the effects of packing structure for granular materials are included. Often, a rule is hypothesized on the evolution of fabric tensors with stress. Work along this line can be found by Oda (1993), Emeriault and Cambou (1996), Wan and Guo (2001), Nemat-Nasser and Zhang (2002), Li and Dafalias (2002), etc. The second category is *microstructural plasticity model*, in which the material parameter is defined at the micro (inter-particle) level. The basic idea is to view the packing as represented by a set of micro-systems. The inelastic behavior of each micro-system is characterized and the overall stress–strain relationship of the packing is obtained from an average of the behaviors of micro-systems. If the micro-systems are regarded as inter-particle planes (or mobilized planes) in the packing, then the approach is similar to that used in modeling elastic behavior. Models based on inter-particle contact planes can be found in Jenkins and Strack (1993), Matsuoka and Takeda (1980), Chang et al. (1989), etc. An alternative way is to view the micro-systems as particle-groups of different configurations. Models developed along this line can be found in Chang et al. (1992a,b), and more recently in Suiker and Chang (2004).

In order to characterize the packing structure, the microstructural plasticity model requires a mathematical or numerical description of the micro-systems, which is not readily available. However, for the cases of treating micro-systems as contact planes or mobilized planes, the approach of estimating the overall behavior by orientational planes can be linked to G.I. Taylor's concept, developed long ago in the slip theory of plasticity for polycrystalline materials by Batdorf and Budianski (1949). These ideas were applied by Pande and Sharma (1982) to rocks and soils in what they called the overlay model, and to concrete by Bazant et al. (1995) in the so-called micro-plane model.

Along these lines, we develop a new stress–strain model considering inter-particle forces and displacements. We incorporate into the model a more recently developed micro–macro links between strain and inter-particle displacements for granular materials (Liao et al., 1997, 2000). The model performance is then evaluated by comparing the predicted and measured triaxial loading results for sand of different void ratios and under different confining stress, in both drained and undrained conditions. Specimens with anisotropy are also studied to demonstrate the advantages of this model.

2. Stress–strain model

In this model, we envision a granular material as a collection of particles. The deformation of a representative volume of the material is generated by the mobilization of contact particles in all orientations. Thus, the stress–strain relationship can be derived as an average of the mobilization behavior of local contact planes in all orientations. For a contact plane in the αth orientation, the local forces f_i^α and the local movements δ_i^α can be denoted as follows: $f_i^\alpha = \{f_n^\alpha, f_s^\alpha, f_t^\alpha\}$ and $\delta_i^\alpha = \{\delta_n^\alpha, \delta_s^\alpha, \delta_t^\alpha\}$, where the subscripts n, s, and t represent the components in the three directions of the local coordinate system. The direction normal to the plane is denoted as n; the other two orthogonal directions, s and t, are tangential to the plane.

The forces and movements at contact planes of all orientations are suitably superimposed to obtain the macroscopic stress strain tensors. The macroscopic stiffness tensor is obtained on the condition that the rate of energy dissipation expressed in terms of the macro stress and strain must be equivalent to that expressed

in terms of micro-forces and movements. In such formulation, it has usually been assumed that the microstructure is statically constrained, which means that the forces on each contact plane are assumed equal to the resolve components of the macroscopic stress tensor. Another equally simple possibility is to assume a kinematically constrained microstructure, in which the movements, rather than the forces on a contact plane, are the resolved components of the macroscopic strain tensor.

The kinematically constrained models are more popularly used in concrete models. The overriding reason for using this approach is that, in case of strain softening, it is easier to construct a stable model using a kinematic rather than a static constraint. However, the kinematic constraint obviously gives a more restrictive deformation pattern, thus provides a stiffer result, especially when granular materials are subjected to high deviatoric stresses (Chang and Misra, 1990). Further discussion on this issue can be found in the work by Chang and Gao (1996), Kruyt and Rothenburg (2002) and Kruyt (2003).

2.1. Inter-particle behavior

2.1.1. Elastic part

The orientation of a contact plane between two particles is defined by the vector perpendicular to this plane. On each contact plane, an auxiliary local coordinate can be established as shown in Fig. 1. The contact stiffness of a contact plane includes normal stiffness, k_n^α, and shear stiffness, k_r^α. The elastic stiffness tensor is defined by

$$f_i^\alpha = k_{ij}^{\alpha e}\delta_j^{\alpha e} \tag{1}$$

which can be related to the contact normal and shear stiffness

$$k_{ij}^{\alpha e} = k_n^\alpha n_i^\alpha n_j^\alpha + k_r^\alpha (s_i^\alpha s_j^\alpha + t_i^\alpha t_j^\alpha) \tag{2}$$

where n, s, t are three orthogonal unit vectors that form the local coordinate system. The vector n is outward normal to the contact plane. Vectors s and t are on the contact plane.

The value of the stiffness for two elastic spheres can be estimated from Hertz–Mindlin's formulation (1969). For sand grains, a revised form was adopted (Chang et al., 1989), given by

$$k_n = k_{n0}\left(\frac{f_n}{G_g l^2}\right)^n; \quad k_t = k_{t0}\left(\frac{f_n}{G_g l^2}\right)^n \tag{3}$$

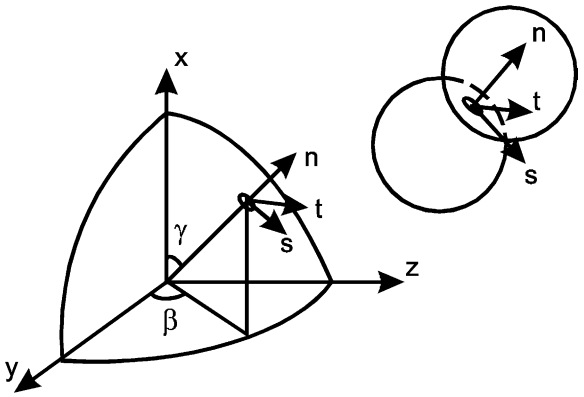

Fig. 1. Local coordinate at inter-particle contact.

where G_g is the elastic modulus for the grains, f_n is the contact force in normal direction. l is the branch length between the two particles. k_{n0}, k_{r0} and n are material constants. For two spherical particles, the branch length is same as particle size $l = d$. Let $n = 1/3$, and

$$k_{n0} = G_g \frac{d}{2} \left(\frac{\sqrt{12}}{1 - \nu_g} \right)^{2/3} \tag{4}$$

Eq. (3) is equivalent to the Hertz–Mindlin's contact formulation.

2.1.2. Plastic part

The elastic sliding behavior between two particles does not have a coupling effect (i.e., there is no shear-induced normal movements). However, the plastic sliding often occurs along the tangential direction of the contact plane with an upward or downward movement, thus the shear dilation/contraction takes place. The stress-dilatancy is a well-known phenomenon in sand (see discussions in the work by Taylor, 1948; Rowe, 1962; Goddard and Bashir, 1990, etc.), and should be correctly modeled. The dilatancy effect can be described by

$$\frac{\mathrm{d}\delta_n^p}{\mathrm{d}\Delta^p} = \frac{T}{f_n} - \tan\phi_0 \tag{5}$$

where ϕ_0 is a material constant which, in most cases, can be considered equal to the internal friction angle ϕ_μ. This equation can be derived by equating the dissipation work due to plastic movements to the friction loss of contact planes in the same orientation. Note that the shear force T and the rate of plastic sliding $\mathrm{d}\Delta^p$ can be defined as

$$T = \sqrt{f_s^2 + f_t^2} \quad \text{and} \quad \mathrm{d}\Delta^p = \sqrt{(\mathrm{d}\delta_s^p)^2 + (\mathrm{d}\delta_t^p)^2} \tag{6}$$

The yield function is assumed to be of Mohr–Coulomb type,

$$F(f_i, \kappa) = T - f_n \kappa(\Delta^p) = 0 \tag{7}$$

where $\kappa(\Delta^p)$ is an isotropic hardening/softening parameter. When $F > 0$, it indicates loading, otherwise unloading. The hardening function is defined by a hyperbolic curve in $\kappa - \Delta^p$ plane, which involves two material constants: ϕ_p and k_{p0}.

$$\kappa = \frac{k_{p0} \tan\phi_\mathrm{p} \Delta^p}{|f_n| \tan\phi_\mathrm{p} + k_{p0}\Delta^p} \tag{8}$$

The value of κ asymptotically approaches $\tan\phi_\mathrm{p}$. The initial slope of the hyperbolic curve is k_{p0}. On the yield surface, under a loading condition, the shear plastic flow is determined by a normality rule applied to the yield function. However, the plastic flow in the direction normal to the contact plane is governed by the stress-dilatancy equation in Eq. (5). Thus the flow rule is non-associated.

2.1.3. Interlocking influence

One of the important elements to consider in granular modeling is the critical state concept. Under critical state, the granular material will remain at a constant volume while it is subjected to a continuous distortion. The void ratio corresponding to this state is e_c.

The critical void ratio e_c is a function of the mean stress. The relationship has traditionally be written as follows:

$$e_\mathrm{c} = \Gamma - \lambda \log(p') \quad \text{or} \quad e_\mathrm{c} = e_\mathrm{ref} - \lambda \log\left(\frac{p'}{p_\mathrm{ref}}\right) \tag{9}$$

and are two material constants and p' is the mean stress of the packing, and $(e_{\text{ref}}, p_{\text{ref}})$ is a reference point on the critical state line.

The internal friction angle ϕ_μ is a constant for the material. However, the peak friction angle, ϕ_p, on a contact plane is dependent on the degree of interlocking by neighboring particles, which can be related to the state of packing void ratio e by

$$\tan\phi_{\text{p}} = \left(\frac{e_{\text{c}}}{e}\right)^m \tan\phi_\mu \tag{10}$$

where m is a material constant (Biarez and Hicher, 1994).

For dense packing, the peak frictional angle ϕ_{p} is greater than ϕ_μ. When the packing structure dilates, the degree of interlocking and the peak frictional angle are reduced, which results in a strain-softening phenomenon.

2.1.4. Elasto-plastic relationship

With the elements discussed above, the final incremental stress–strain relations of the material can be derived that includes both elastic and plastic behavior, given by

$$\dot{f}_i^\alpha = k_{ij}^{\alpha p}\dot{\delta}_j^\alpha \tag{11}$$

Detailed expression of the elasto-plastic stiffness tensor is given in Appendix A.

2.2. Stress–strain relationship

2.2.1. Macro–micro relationship

The stress–strain relationship for an assembly can be determined from integrating the behavior of inter-particle contacts in all orientations. During the integration process, a relationship is required to link the macro and micro-variables. Using the static hypotheses proposed by Liao et al. (1997), we obtain the relation between the macro strain and inter-particle displacement (here, we do not consider the finite strain condition)

$$\dot{u}_{j,i} = A_{ik}^{-1}\sum_{\alpha=1}^{N}\dot{\delta}_j^\alpha l_k^\alpha \tag{12}$$

where $\dot{\delta}_j$ is the relative displacement between two contact particles and the branch vector l_k is the vector joining the centers of two contact particles. It is noted that contact particles include both direct contact and indirect contact of neighboring particles associate with a Voronoi polyhedron as discussed by Cambou et al. (2000). For convenience, we let N be the total number of contact orientations. The variables $\dot{\delta}_j^\alpha$ and l_k^α are defined respectively as the averaged values of $\dot{\delta}_j$ and l_k for all contacts belong to the αth orientation. The fabric tensor in Eq. (12) is defined as

$$A_{ik} = \sum_{\alpha=1}^{N} l_i^\alpha l_k^\alpha \tag{13}$$

Using the principle of energy balance and using Eq. (14), the mean force on the contact plane of each orientation are

$$\dot{f}_j^\alpha = \dot{\sigma}_{ij}A_{ik}^{-1}l_k^\alpha V \tag{14}$$

In Eq. (14), the stress increment $\dot{\sigma}_{ij}$ can be obtained by the contact forces and branch vectors for contacts in all orientations (Christofferson et al., 1981; Rothenburg and Selvadurai, 1981)

$$\dot{\sigma}_{ij} = \frac{1}{V}\sum_{\alpha=1}^{N} \dot{f}_j^{\alpha} l_i^{\alpha} \tag{15}$$

Applying the defined contact force in Eqs. (14) and (15) is unconditionally satisfied.

2.2.2. Computation scheme

The problem is defined by the following:

Initially, we know the global variables (σ_{ij} and ε_{ij}) for the assembly and the local variables (f_j^{α} and δ_j^{α}) for each contact orientation. For a given loading increment, which can be stress control, strain control or mixed mode, out of the 12 variables ($\Delta\sigma_{ij}$ and $\Delta\varepsilon_{ij}$), six of them are unknown. The objective is to determine all global variables (σ_{ij} and ε_{ij}) and local variables (f_j^{α} and δ_j^{α}) at the end of load increment. For a system with N inter-particle orientations, the number of unknown is $3N$ for f_j^{α} and $3N$ for δ_j^{α}. The total number of unknown is $3N + 3N + 6$.

The following constraints must be satisfied:

(1) The local constitutive equation, i.e. Eq. (11). Since there are three equations for each contact plane orientation, the total number of equations is $3N$, N being the total number of inter-particle orientations.
(2) Static hypothesis between global stress and local forces, i.e. Eq. (14): the number of equations is $3N$.
(3) Strain definition between global strain and local displacement, i.e. Eq. (12). The number of equations is six (strain is symmetric).

The total number of unknowns is the same as the total number of equations. Therefore, the solution can be determined.

Using Eqs. (11), (12), and (14), the following relationship between stress and strain can be obtained:

$$\dot{u}_{i,j} = C_{ijmp}\dot{\sigma}_{mp}; \quad \text{where } C_{ijmp} = A_{ik}^{-1}A_{mn}^{-1}V\sum_{\alpha=1}^{N}\left(k_{jp}^{\mathrm{ep}}\right)^{-1} l_k^{\alpha} l_n^{\alpha} \tag{16}$$

The summation in Eq. (16) can be replaced by an integral over orientations. The integral can lead to a closed-form solution for the elastic modulus of randomly packed equal-size particles (Chang et al., 1995). However, in the elastic plastic behavior, due to the non-linearity nature of the local constitutive equation, a numerical calculation with iterative process is necessary to carry out the summation in Eq. (16). In order to facilitate the numerical calculation, the orientations are selected to coincide with the locations of Gauss integration points in a spherical coordinate. Summation over these orientations with the Gauss weighting factor for each orientation is equivalent to determining the integral over orientations. We found that the results were more accurate by using a set of fully symmetric integration points. From a study of the performance of using different numbers of orientations, we found $N \geqslant 74$ to be adequate.

For a strain-controlled test, Eq. (16) is not useful especially at the after-peak range of strain-softening. In this case, a method of "elastic predictor–plastic corrector" was adopted to obtain the solution. For a mix-mode loading condition, additional process of distributing the unbalance stresses was also needed. The detailed procedure is not included here.

2.3. Summary of parameters

One can summarize the material parameters as:

- Normalized contact number per unit volume: Nl^3/V
- mean particle size, d

- Inter-particle elastic constants: k_{n0}, k_{t0} and n;
- Inter-particle friction angle: ϕ_μ and m;
- Inter-particle hardening rule: k_{p0} and ϕ_0;
- Critical state for the packing: λ and Γ or e_{ref} and p_{ref}.

Besides critical state parameters, all other parameters are for inter-particles. Standard values for k_{p0} and ϕ_0 are the following: $k_{p0} = k_n$ and $\phi_0 = \phi_\mu$ and a typical ratio $k_{t0}/k_{n0} = 0.5$ can be generally assumed. Therefore, only six parameters have to be derived from experimental results and they can all be determined from the stress–strain curves obtained from drained compression triaxial tests.

Regarding the effect of the particle size, Eq. (4) shows that the inter-particle stiffness k_{n0} is influenced by the mean particle size. Since in this model, the tangential stiffness k_{t0} and the plastic stiffness k_{p0} are directly related to k_{n0}, they are also particle size dependent. Considering an assembly of particles under an externally applied stress, according to Eqs. (3) and (4) and using the expression of contact force in terms of external stress, the inter-particle stiffness is proportional to the mean particle size (see Liao et al., 2000):

$$k_n \propto G_{\text{g}}^{1-n} d \left(\frac{Nl^3}{V}\right)^{-n} \sigma^n \tag{17}$$

Although the magnitude of the inter-particle stiffness is dependent on the particle size, the elastic shear modulus of a packing is not particle size dependent. This can be derived by the fact that the shear modulus of a packing is proportional to k_n/d, thus it leads to (Liao et al., 2000):

$$G \propto G_{\text{g}}^{1-n} (\sigma)^n \left(\frac{Nl^3}{V}\right)^{1-n} \tag{18}$$

Note that the dimensionless density factor Nl^3/V is a function of the void ratio only. Thus, the shear modulus of the packing is not particle size dependent.

3. Results of numerical simulation

3.1. Drained triaxial tests

A series of drained triaxial tests on coarse Hostun sand undertaken by Bouvard (1982) have been reported and analyzed by Biarez and Hicher (1994). The tests were performed at different confining pressures on samples prepared at different initial void ratios. Typical results are presented in Fig. 2, which shows the triaxial testing results for both dense and loose specimens made of Hostun sand. The stress strain curves are plotted for three different confining stresses in Fig. 2a. The void ratio change with respect to strain is plotted in Fig. 2b.

One can see the combined influence of the initial void ratio and of the mean effective stress on the stress–strain curves and the volumetric change. The stress–strain curve has a peak corresponding to the dilatancy of the sample, which increases with its initial relative density. For dilatant materials, the deviatoric stress reduces after peak and towards a constant state of stress for a constant void ratio corresponding to the critical state. In practice, it is difficult to reach this state because of strain localization, especially in dense materials. It is possible however to limit the effect of the localization by reducing the slenderness of the specimen and by taking measures to minimize the friction between the rigid end platens and the specimen. This was done in the tests presented here, which allowed the strain localization to delay at large deformations. The critical state could therefore be determined with sufficient accuracy (Biarez and Hicher, 1994).

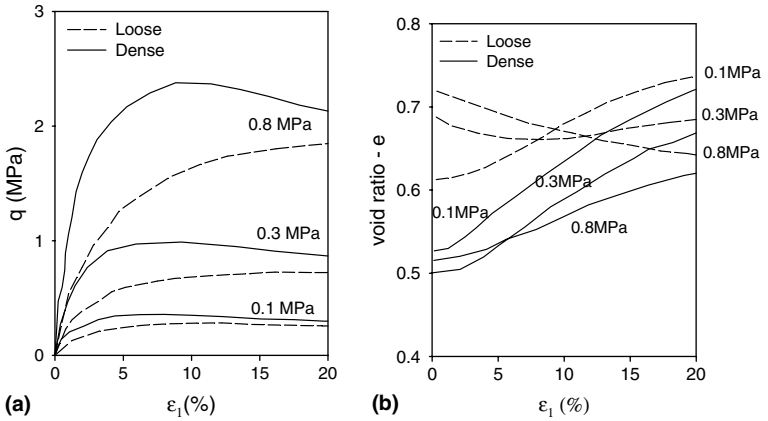

Fig. 2. Experimental results: (a) stress vs. strain curves, and (b) void ratio vs. strain curves (Bouvard, 1982).

The model needs a small number of input parameters such as mean particle size, particle stiffness, inter-particle friction, initial porosity tensor, and initial degree of interlocking. The model performance is demonstrated by comparing the predicted and measured macro behavior.

The mean size of the particle for Hostun sand is $d = 1.3\,\text{mm}$. The inter-particle elastic constant k_{n0} is assumed 61 000 N/mm. The normalized contact number per volume Nl^3/V can be obtained by matching the predicted and experimentally measured elastic modulus for specimens with different void ratios. The calculated relationship of Nl^3/V versus void ratio for Huston sand is shown in Fig. 3. The relationship for regular packing of equal sized spheres is also plotted in Fig. 3 for comparison. The evolution of Nl^3/V due to new contact generation with neighbor particles was not considered.

The value of k_{t0}/k_{n0} is commonly about 0.4, corresponding to a Poisson's ratio for Hostun sand $= 0.2$ and the exponent $n = 0.5$ (Biarez and Hicher, 1994). From results in Fig. 2, we were able to derive the values of the two parameters corresponding to the position of the critical state in the e–p' plane: $\lambda = 0.16$ and $p_{\text{ref}} = 0.1\,\text{MPa}$ for $e_{\text{ref}} = e_{\max} = 0.81$. The friction angle ϕ_μ was also determined from the stress state corresponding to the critical state: $\phi_\mu = 33°$. The equation governing the dilatancy rate requires the determination of the parameter ϕ_0. This parameter represents the concept of "phase transformation" as defined by

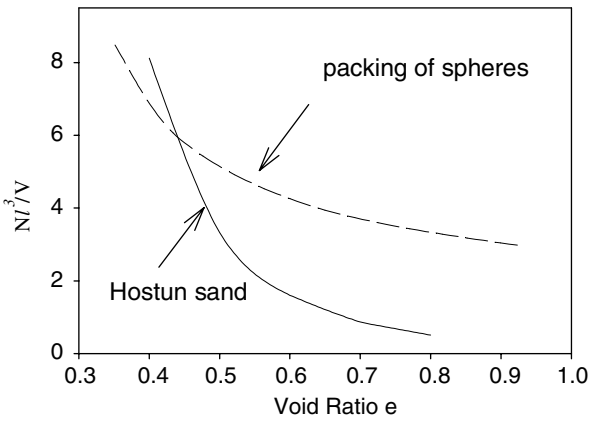

Fig. 3. Inter-particle contact per unit volume vs. void ratio.

Ishihara and Towhata (1983) or "characteristic state" as defined by Luong (1980). A value of $\phi_0 = \phi_\mu$ was retained in accordance with the fact that, for contractant samples, the critical state was reached for the maximum value of the deviatoric stress, i.e. the sample was contractant all the way to the critical state.

The peak friction angle is not an intrinsic parameter, but varies with the void ratio according to Eq. (10). A value of $m = 0.6$ was determined from the test results. The values of k_{p0} are directly connected to the elastic properties by considering the relation: $k_{p0} = ak_n$. Here we simply considered that $k_{p0} = k_n$.

The set of parameters for coarse Hostun sand is presented in Table 1.

The numerical simulations are presented in Fig. 4. A reasonable simulation of the behavior of coarse Hostun sand at various mean effective stresses and various initial void ratios can be obtained with a single set of model parameters, capturing both the contractive and dilative behavior of the sand as well as the influence of this contractant or dilatant behavior on the stress–strain curves and on the maximum strength. For large deformations, the curves corresponding to the same confining stress and different initial void ratios converge towards an identical stress state and void ratio, in accordance with the definition of the critical state.

The set of parameters in Table 1, which can be directly determined from the experimental curves, has the advantage of being commonly used in the soil mechanics community: elastic stiffness, friction angle and critical state parameters.

Fig. 5 presents a set of measured stress–strain behaviors showing the influence of the initial void ratio. The representation of the curves obtained by Biarez and Hicher (2002) from a comparison of results on different sands at different initial void ratios. They show the correspondence between the stress–strain curve and the volumetric change for contactant and dilatant materials. Fig. 6 presents a set of numerical results obtained with the set of parameters from Table 1 with different initial void ratios, corresponding to relative densities between 0.05 and 1. Both stress–strain relations and volume changes are in agreement with the experimentally measured curves in Fig. 5.

Table 1
Model parameters for coarse Hostun sand

e_{ref}	p_{ref} (MPa)	λ	ϕ_μ (°)	ϕ_0 (°)	m
0.81	0.1	0.16	33	33	0.6

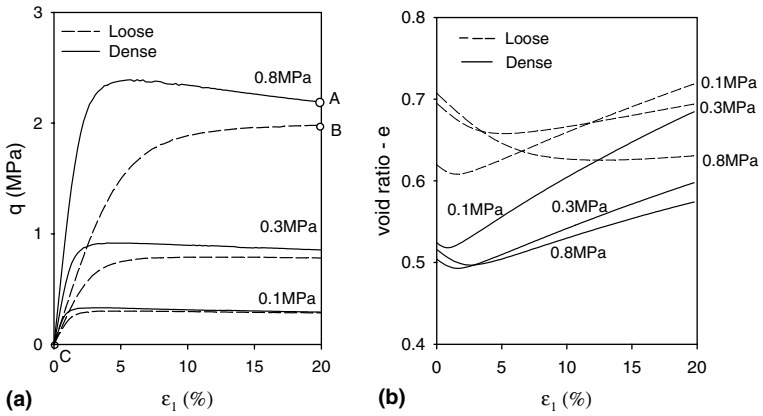

Fig. 4. Model predictions: (a) stress vs. strain curves, and (b) void ratio vs. strain curves.

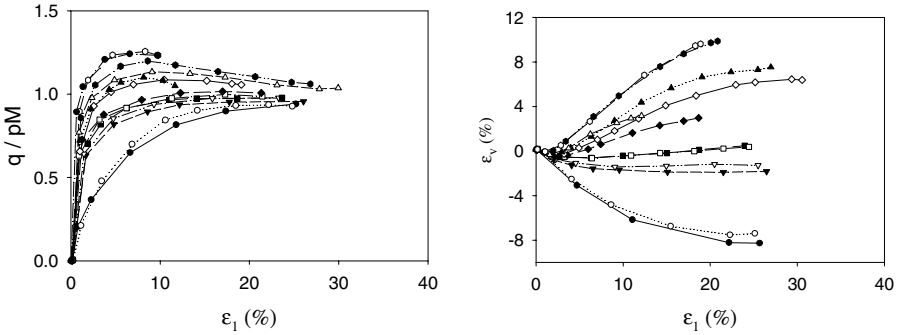

Fig. 5. Measured test results from various types of sand and densities.

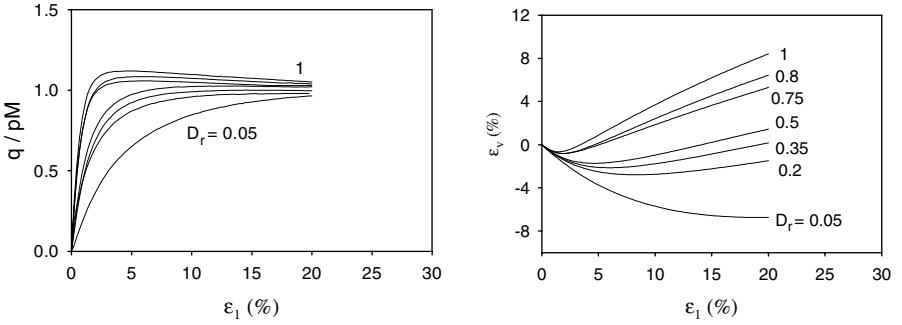

Fig. 6. Model predictions for various relative densities.

3.2. Undrained triaxial tests

Undrained triaxial tests have also been simulated, under the same set of parameters. The experimental results are plotted in Fig. 7 compared with the predicted results in Fig. 8. One can see that for strongly contractive materials, i.e. small values of the relative density, a maximum strength is obtained in the q–ε_1 plane followed by a decrease of the deviatoric stress down to a minimum strength which is almost zero

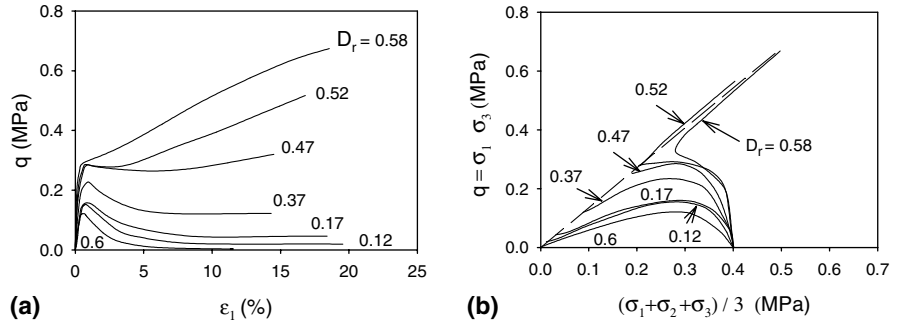

Fig. 7. Experimental results for undrained triaxial tests: (a) stress–strain curves, and (b) stress paths (Bouvards).

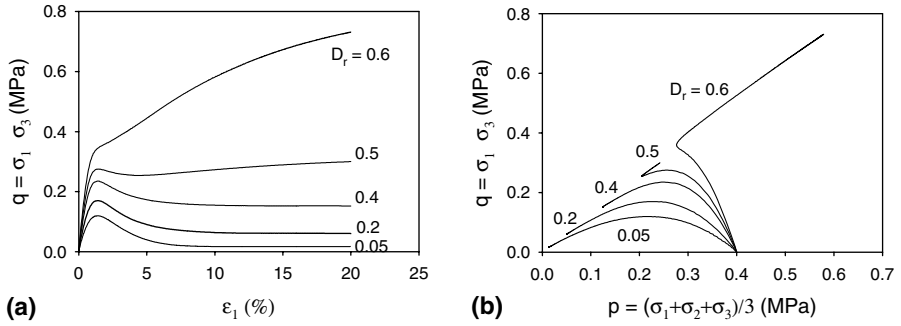

Fig. 8. Model predictions for undrained triaxial tests: (a) stress–strain curves, and (b) stress paths.

for a relative density close to zero. This represents the phenomenon called static liquefaction. For slightly higher relative densities, the same pattern is first observed but it is then followed by an increase of the deviatoric stress up to the ultimate strength at large deformations, corresponding to the critical state. For dilatant materials, the deviatoric stress increases monotonically up to an ultimate stress achieved at large deformations when the critical state is reached. These different evolutions can be related to the stress paths followed in a p', q plane: continuous decrease of the mean effective stress for strongly contractant materials, decrease followed by an increase up to the critical state for dilatant materials. These results indicate that in undrained condition also, the model is capable of capturing the general trend observed for contractive and dilative sands (Hicher, 1998).

3.3. Inherent anisotropy

One of the main interests of the model is its capacity to take into account a structural anisotropy. In fact, the decomposition of the constitutive equations along a set of planes allows to formulate the dependency of the parameters with respect to the orientation. If we do so, we can obtain a response which depends on the loading orientation in relation to the direction of material anisotropy. Several studies have demonstrated the influence of inherent anisotropy on the mechanical response of sands. When prepared in the gravitational field, granular materials may have a packing structure anisotropy even for spherical grains. The anisotropy can be characterized by a fabric tensor, defined by

$$[F_{ij}] = \begin{bmatrix} F_{11} & 0 & 0 \\ 0 & F_{22} & 0 \\ 0 & 0 & F_{33} \end{bmatrix} = F_{\text{ave}} \begin{bmatrix} 1+a_0 & 0 & 0 \\ 0 & 1-\dfrac{a_0}{2} & 0 \\ 0 & 0 & 1-\dfrac{a_0}{2} \end{bmatrix} \tag{19}$$

where $F_{\text{ave}} = (F_{11} + F_{22} + F_{33})/3$ and a_0 is the parameter showing the degree of anisotropy. It was found (see Chang and Misra, 1990) that the tensor in Eq. (19) matches the continuous function given below:

$$F(\gamma, \beta) = \frac{F_{\text{ave}}}{4\pi}\left(1 + \frac{a_0}{4}(3\cos 2\gamma + 1)\right) \tag{20}$$

where F is a variable function of the orientation defined by the two angles γ, β in a spherical coordinates (see Fig. 1). In the case of symmetry around the major axis, F is only a function of γ. Eq. (20) is a truncated form of the spherical harmonic expansion up to second-order terms. An example of the function F with different values of a_0 is shown in Fig. 9.

For a soil layer, the inherent anisotropy in Eq. (20) represents a distribution function, which has symmetry about its major axis that often coincides with the vertical direction. The anisotropy of the packing

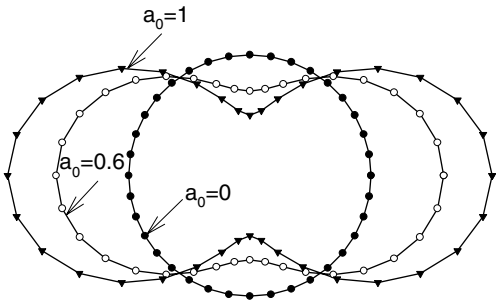

Fig. 9. Schematic plot for inherited anisotropy.

structure creates an anisotropy of the mechanical behavior whose directions are identical to those of the geometric anisotropy. Several studies have shown that the stress–strain behavior reflects the inherent anisotropic fabric in sand specimens. It has been found that the stiffness is larger when the direction of the major principal stress coincides with the principal direction of fabric tensor. For sands prepared by pluviation inside a mould, the stress–strain curve presents a stiffer slope when the major principal stress is applied perpendicular to the bedding plane and, on the contrary, a lower slope when the major principal stress is applied in the direction of the bedding plane.

Results of this sort were presented by Ochai and Lade (1983) on Cambria sand (long grains) prepared by pouring vertically and shaking sand grains into a tilted mould. The cube in Fig. 10 represents a specimen; the shaded plane is the plane of pluviation. The specimen is cross anisotropic. Properties in directions 2 and 3 are the same, but different from that in direction 1. The principal material axis for the specimen is perpendicular to the plane of pluviation. Photographs were taken of horizontal and vertical sections through central regions of the specimen. Measurements of grain orientation were made and reported on a rose diagram (Fig. 10). They showed that the grains had distinctly preferred orientations in the vertical section, but

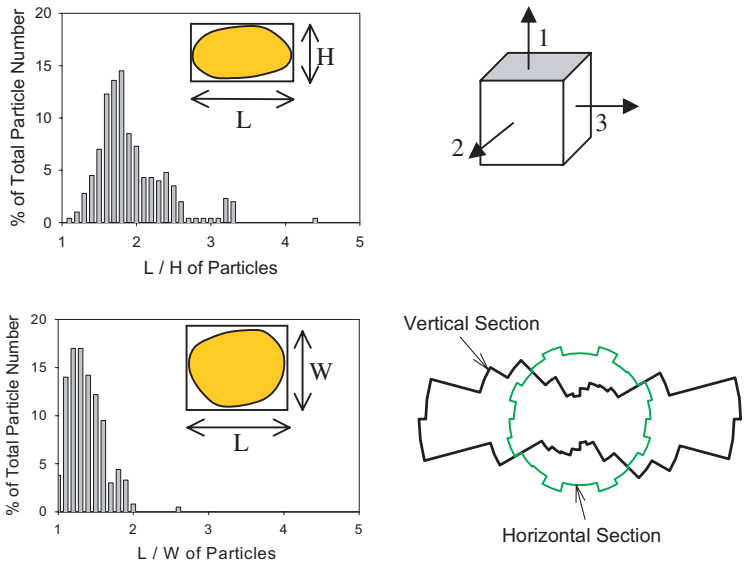

Fig. 10. Distributions for grain shape and grain orientation.

random orientations in the horizontal section. Grain shape is characterized by the length of its three axes, L, H, and W. The distribution of L/H and L/W are also plotted in Fig. 10. The average ratio of the major length to the minor length is 1.8. Because the present model does not explicitly consider the factor of grain shape, in this simulation, the anisotropy due to grain shape is reflected on the parameters, Nl^3/V, k_{p0}/k_{n0}, and ϕ_μ, as described in the subsequent paragraphs.

Triaxial compression tests were performed on Cambria sand specimen prepared as described above and loaded in two different ways: (1) coaxial loading and (2) non-coaxial loading, as shown in Fig. 11. In the first case, the loading direction coincides with the principal material axis. In the second case, they are perpendicular. The measured results presented in Fig. 12 for various confining pressures show clear differences according to the direction of loading. The curves tend to approach each other at large strains, even if the authors reported slight differences in peak friction angles, varying from 2° for $\sigma_3 = 50\,\text{kPa}$ to 0.5° for $\sigma_3 = 400\,\text{kPa}$.

In order for the model to be able to reflect the initial anisotropy of the specimen, the values of the parameters representing the behavior at the micro-scale were made to depend on the orientation of the selected planes. In this case, a cross-anisotropy can be assumed around an axis of symmetry corresponding to the vertical direction.

The mean particle diameter is 0.15 mm. The inter-particle elastic constant k_{n0} is assumed to be 20 500 N/mm. The initial void ratio of the specimens was 0.53–0.54. In this range of void ratio, the contact density Nl^3/V is assumed to be 2.5. According to the rose diagram for the grain orientation in Fig. 10, it is expected

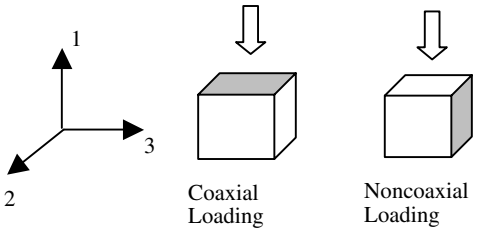

Fig. 11. Coaxial and non-coaxial loading conditions.

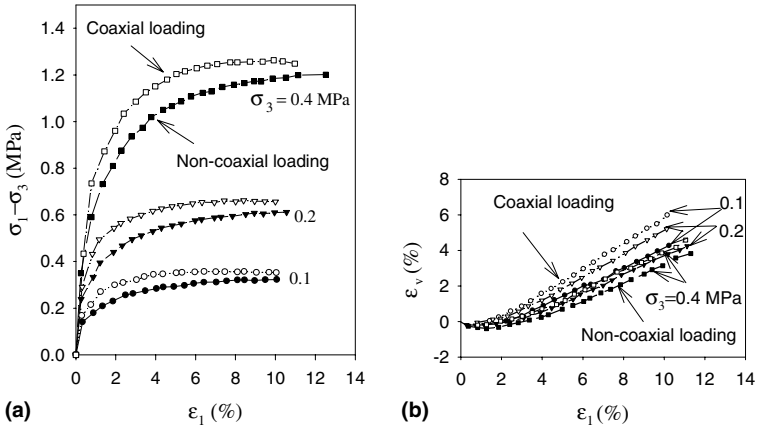

Fig. 12. Cubical triaxial experimental results: (a) stress–strain curves, and (b) volumetric strain vs. axial strain curves.

that the distribution of Nl^3/V is symmetric about the vertical axis. Its degree of anisotropy is estimated to be 0.2. Typical value of $k_{t0}k_{n0} = 0.5$ and the exponent $n = 0.5$ were considered.

For a packing of non-spherical particles, it is not sufficient to specify only the anisotropy a_0 on the contact number, because other factors such as contact area and grain shape also contribute to the material anisotropy. In addition, in this simulation, we applied anisotropy directly to the plastic–elastic stiffness ratio k_{p0}/k_{n0} and the friction angle ϕ_μ. The observed anisotropic mechanical behavior can be predicted reasonably well by imposing orientational dependency on the following three inter-particle parameters.

(1) The average contact density $Nl^3/V = 2.5$ with a degree of anisotropy $(a_0)_{k_n} = 0.2$
(2) The average ratio of $k_{p0}/k_{n0} = 0.43$ with a degree of anisotropy $(a_0)_{k_{p0}}/k_{n0} = 1.32$
(3) The average $\phi_\mu = 41.3^0$ with a degree of anisotropy $(a_0)_{\phi_\mu} = 0.45$

Mean values and degrees of anisotropy of the parameters were determined by curve fitting, using the experimental results obtained from the triaxial tests at $\sigma_3 = 0.2$ MPa for vertical and horizontal loading.

Since the results presented in the paper were not sufficient for determining the critical state for Cambria sand, usual values for this type of sand were assumed (Biarez and Hicher, 1994). The parameter values are presented in Table 2. They were determined from the two triaxial tests at $\sigma_3 = 200$ kPa. The value of m was determined from the evolution of the peak friction angle with the confining pressure.

The results of the numerical simulations are presented in Fig. 13. They are in good agreement with the experimental results in Fig. 12. The general trend is well captured by the model. Specimen appear stiffer when the compressive stress is applied in the direction of deposition. The volumetric strain behavior also reflects the initial anisotropy. The specimen loaded in a vertical direction exhibit a smaller amount of compression and larger rates of dilation than those loaded in a horizontal direction, as can also be observed on the experimental curves.

Table 2
Parameters for cross-anisotropic Cambria sand

e_{ref}	p_{ref} (MPa)	λ	ϕ_0 (°)	m
0.83	0.1	0.05	32	0.05

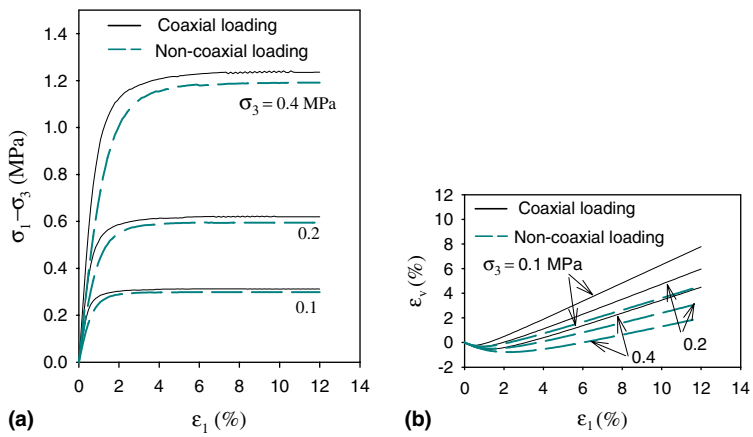

Fig. 13. Model predictions: (a) stress–strain curves, and (b) volumetric strain vs. axial strain curves.

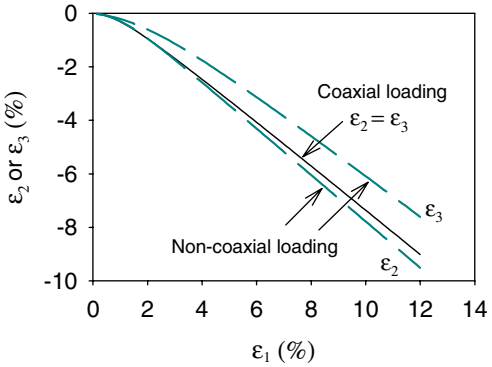

Fig. 14. Medium and minor principal strains in coaxial and non-coaxial loading case.

Since the sample is cross isotropic, under the loading in direction 1, the normal strain in directions 2 and 3 are the same for the coaxial case but different for the non-coaxial loading case. The strains are plotted in Fig. 14 for the case of $\sigma_3 = 0.2$ MPa. In the non-coaxial loading case, the strain in direction 2 is larger than that in direction 3.

In order to have insights on the deformation behavior between particles, we examined the particles oriented in four directions as the branch vectors shown in Fig. 15. The branch vectors are located on the 1–3 plane of the coordinate system. The angle γ is measured between the 1-axis and the branch vector. We selected four values of $\gamma = 0$, 18, 45, 72 degrees. Fig. 16 shows the evolution of normal and shear stresses with shear strain on the four planes. Local strains and stresses (see definitions in Appendix B) rather than inter-particle forces and displacements were plotted in order to obtain a more direct comparison between the local behavior and the overall stress–strain behavior. On plane "*d*", perpendicular to the loading direction, the shear traction is zero. Fig. 16 shows that plane "*c*" is mobilized to about 1%, then the movement is stopped. Plane "*a*" continues to be mobilized to about 3.5% and plane "*a*" continues all the way to the end of test. This indicates that in the beginning of loading, all planes are mobilized. Some planes stopped to mobilize as the loading increases. Further deformation is obtained by the mobilization of remaining planes. The total number of mobilizable planes continues to decrease. At peak stress, most planes stopped moving. Only a few remaining planes are responsible for the deformation.

Fig. 16 also shows the normal strain versus shear strain for each plane. Plane "*d*" experiences only normal strain without shear. Plane "*c*" experiences shear contraction while planes "*a*" and "*b*" experience shear dilation. The difference between coaxial and non-coaxial loading is quite pronounced in the local behavior.

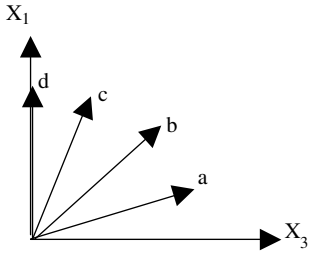

Fig. 15. Four inter-particle orientations located on the X_1–X_3 plane of the coordinate system.

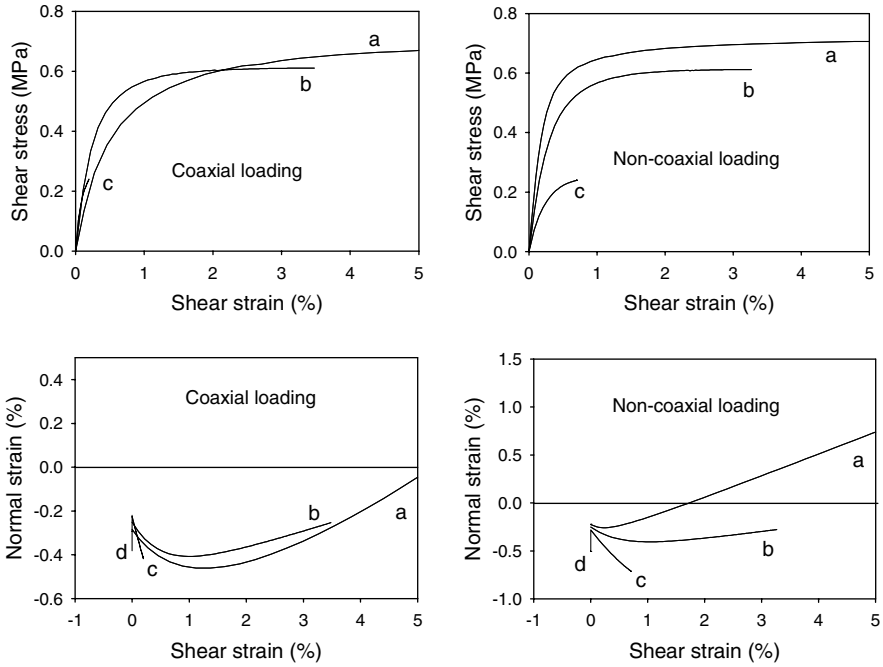

Fig. 16. Comparison of behaviors on four different inter-particle planes for both coaxial and non-coaxial loading case.

To evaluate the evolution of strain heterogeneity predicted in this model, we selected three load stages to observe the orientational distributions of local stress and local strain. For the triaxial test ($\sigma_3 = \sigma_2 = 0.2$ MPa) with coaxial loading case, the stresses σ_1 for the three selected stages are 0.60, 0.70, and 0.75 MPa. The static hypothesis is used to determine the normal stresses on the planes of various orientations on the 1–3 plane, which are plotted in Fig. 17 for the three load stages marked as a, b, and c. It verifies that the predicted local stresses are identical to that of static hypothesis adopted in this model. The predicted local strains on planes of various orientations are plotted in Fig. 18 for the three load stages. Compared with the local strains based on the kinematic hypothesis, it is obvious that the predicted local

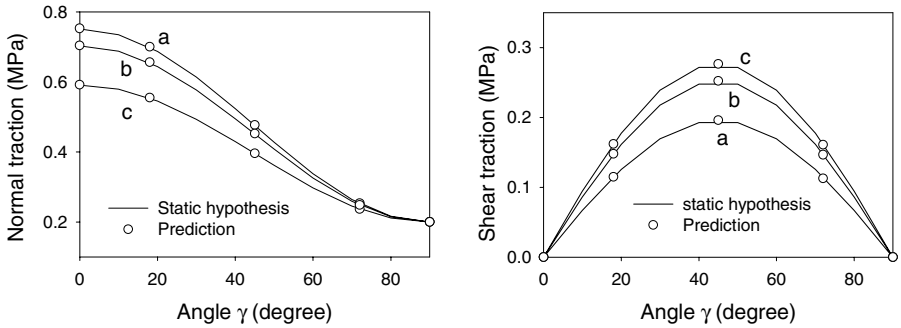

Fig. 17. Comparison of predicted stress tractions on inter-particle planes with that obtained from static hypothesis for three load stages.

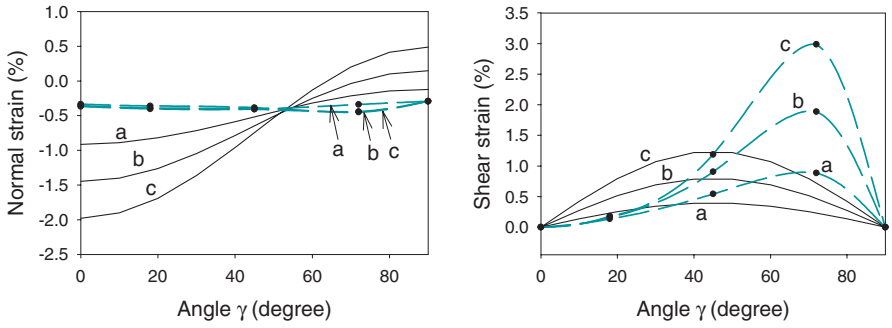

Fig. 18. Comparison of predicted strain on inter-particle planes with that obtained from kinematic hypothesis for three load stages.

strains are highly heterogeneous and do not conform to an uniform state of strain. The current model shows that the normal strains are much smaller than that obtained from kinematic hypothesis and the shear strains are much larger in certain orientations. The predicted qualitative behavior is in agreement with the experimental measurements from computer tomography (Chang et al., 2003).

4. Summary and conclusion

The microstructural approach is attractive conceptually, because it dispenses in having to deal with relations between the stress and strain tensors. Rather, we need to describe only a simple relation between the vectors of forces and relative displacements on a contact plane, which thus requires fewer material parameters. The stress and strain tensors are automatically obtained by integration over all spatial orientations. Aside from modeling simplicity, the microstructural approach is more realistic, especially for the stress-induced or inherent anisotropy. Furthermore it can capture the slip deformation on each plane, thus developing automatically the anisotropy induced from stress application.

In the model, a simple elastic–plastic behavior was assumed on each contact plane. The elastic part is based on the Hertz–Mindlin's contact formulation, while the plastic part is based on a Mohr–Coulomb friction law with an isotropic hardening assumption and a non-associated flow rule. For the whole packing, a critical state behavior is assumed at large deformations and the friction angle on each plane is related to the actual void ratio compared to the critical void ratio at the same state of stress. A strain softening behavior can therefore be obtained for dense materials. On the whole, the model requires a limited number of parameters, which can easily be determined from conventional triaxial testing.

The ability of the model to reproduce the main features of the sand behavior has been demonstrated. Model simulations were compared with drained triaxial tests results at different initial void ratios and different confining stresses leading to contractant or dilatant behavior of the sand specimens. A good accuracy was obtained between numerical simulations and experimental results, by use of a unique set of parameters. Simulations of undrained triaxial tests with the same set of parameters demonstrated that the model is capable of reproducing the general trend for both loose and sense sands.

An inherent anisotropy can easily be introduced by giving an orientation dependency to the parameters. In the examples presented, the inherent anisotropy of deposited sand was reproduced by making the inter-particle stiffness as well as the friction angle cross-anisotropic. In this way, the model was able to reproduce the differences observed in the stress–strain relationship and the volume change during drained triaxial loading in vertical and horizontal directions.

Appendix A

Follow the consistency equation, $dF = 0$, which yield

$$dF = \frac{\partial F}{\partial f_i} df_i + \frac{\partial F}{\partial \kappa} \frac{\partial \kappa}{\partial \delta_i^p} d\delta_i^p = 0 \tag{A.1}$$

For the specific yield function given in Eqs. (7) and (A.1) can be expressed as

$$dF = \frac{\partial F}{\partial f_i} df_i - \frac{\partial \kappa}{\partial \Delta^p} \frac{\partial \Delta^p}{\partial \delta_i^p} d\delta_i^p = 0 \tag{A.2}$$

The derivatives in Eq. (A.2) can be obtained from the definition of F, κ and Δ^p previously defined. The plastic shear displacement is obtained in accordance with the associated flow rule (i.e. $d\delta_j^p = \lambda \frac{\partial F}{\partial f_j}$) and the plastic normal displacement is obtained by dilatancy equation (5). The three components can be related to the scalar plastic displacement $d\Delta^p$, which is defined in Eq. (6). We define the plastic flow vector ξ_i such that

$$d\delta_j^p = \Delta^p \xi_j \tag{A.3}$$

Or in vector form,

$$\begin{Bmatrix} d\delta_n^p \\ d\delta_s^p \\ d\delta_t^p \end{Bmatrix} = d\Delta^p \begin{Bmatrix} T/f - \tan\phi_\mu \\ f_s/T \\ f_t/T \end{Bmatrix} \tag{A.4}$$

The displacement is assumed to consist of elastic component and plastic component. The force can be calculated from the elastic component by

$$df_i = k_{ij}^e (d\delta_j - d\delta_j^p) \tag{A.5}$$

Substitute Eq. (A.5) into Eq. (A.1), then using Eq. (A.4), we obtain

$$\lambda = \frac{\frac{\partial F}{\partial f_i} k_{ij}^e d\delta_j}{\frac{\partial F}{\partial f_i} k_{ij}^e \xi_j + \frac{\partial \kappa}{\partial \Delta^p} \frac{\partial \Delta^p}{\partial \delta_j^p} \xi_j} \tag{A.6}$$

Substitute Eq. (A.6) into Eq. (A.5), the incremental force–displacement relationship for two particles under sliding can be expressed as

$$df_i = k_{ij}^{ep} d\delta_j \tag{A.7}$$

where

$$k_{ij}^{ep} = k_{ij}^e - \frac{k_{in}^e \frac{\partial F}{\partial f_n} \xi_m k_{mj}^e}{\frac{\partial F}{\partial f_m} k_{mn}^e \xi_n + \frac{\partial \kappa}{\partial \Delta^p} \frac{\partial \Delta^p}{\partial \delta_m^p} \xi_m} \tag{A.8}$$

Appendix B

Considering the system as a set of mobilized planes and using the variables of local traction τ_i and local strain γ_i for each plane. For a unit volume, the work due to virtual displacement is given by

$$\frac{1}{V}\sum_{\alpha} f_j^{\alpha}\Delta\delta_j^{\alpha} = \frac{1}{N}\sum_{\alpha}\tau_j^{\alpha}\Delta\gamma_j^{\alpha} \tag{B.1}$$

N is the total number of orientations considered (i.e., α is summed from 1 to N). Note that the local strain can be related to the relative displacement between two particles by $\Delta\gamma_j^{\alpha} = \Delta\delta_j^{\alpha}/l^{\alpha}$, thus the traction is related to inter-particle force by

$$\tau_j^{\alpha} = \frac{N}{V} f_j^{\alpha} l^{\alpha}. \tag{B.2}$$

References

Batdorf, S.B., Budianski, B., 1949. A mathematical theory of plasiticity based on concept of slip. NACA Tech note TN, 1871.

Bazant, Z.P., Xiang, Y., Ozbolt, J., 1995. Nonlocal microplane model for damage due to cracking. Proceedings of Engineering Mechanics 2, 694–697.

Biarez, J., Hicher, P.Y., 1994. Elementary Mechanics of Soil Behaviour. Balkema, p. 208.

Biarez, J., Hicher, P.Y., 2002. mécanismes de déformation des sols. In: Hicher, P.Y., Shao, J.F. (Eds.), Elastoplasticité des sols et des roches, modèles de comportement des sols et des roches 1, Hermes-Lavoisier, pp. 47–89.

Bouvard, D., 1982. rhéologie des milieux pulvérulents: étude expérimentale et identification d'une loi de comportement. Thèse de Docteur_Ingénieur, Université de Grenoble.

Cambou, B., Dedecker, F., Chaze, M., 2000. Relevant local variables for the change of scale in granular materials. In: Dimitrios, Kolymbas (Ed.), Constitutive Modelling of Granular Materials. Springer, Berlin, pp. 275–290.

Chang, C.S., 1988. Micromechanical modeling of constructive relations for granular material. In: Satake, M., Jenkins, J.T. (Eds.), Micromechanics of Granular Materials, pp. 271–279.

Chang, C.S., Gao, J., 1996. Kinematic and static hypotheses for constitutive modeling of granulates considering particlerotation. Acta Mechanica 115 (1–4), 213–229.

Chang, C.S., Misra, A., 1990. Application of uniform strain theory to heterogeneous granular solids. Journal of Engineering Mechanics, ASCE 116 (10), 2310–2328.

Chang, C.S., Kabir, M., Chang, Y., 1992a. Micromechanics modelling for the stress strain behavior of granular soil II: evaluation. Journal of Geotechnical Engineering, ASCE 118 (12), 1975–1994.

Chang, C.S., Misra, A., Acheampon, K., 1992b. Elastoplastic deformation of granulates with frictional contacts. Journal of Engineering Mechanics, ASCE 118 (8), 1692–1708.

Chang, C.S., Chao, S.C., Chang, Y., 1995. Estimates of mechanical properties of Granulates with Anisotropic random packing structure. International Journal of Solids and Structures 32 (14), 1989–2008.

Chang, C.S., Matsushima, T., Lee, X., 2003. Heterogeneous strain and bonded Granular Structure change in triaxial specimen studied by computer tomography. Journal of Engineering Mechanics 129 (11), 1295–1307.

Chang, C.S., Misra, A., Weeraratne, S.P., 1989. A slip mechanism based constitutive model for granular soils. Journal of Engineering Mechanics, ASCE 115 (4), 790807.

Chang, C.S., Sundaram, S.S., Misra, A., 1989. Initial moduli of particulate mass with frictional contacts. International Journal for Numerical and Analytical Methods in Geomechanics 13 (6), 626–641.

Christofferson, J., Mehrabadi, M.M., Nemat-Nassar, S., 1981. A micromechanical description on granular material behavior. ASME Journal of Applied Mechanics 48, 339–344.

Emeriault, F., Cambou, B., 1996. Micromechanical modelling of anisotropic non-linear elasticity of granular medium. International Journal of Solids and Structures 33 (18), 2591–2607.

Goddard, J.D., Bashir, Y.M., 1990. On Reynolds dilatancy. In: De Kee, D., Kaloni, P.N. (Eds.), Recent Development in Structured Continua, vol. II. Longman's, London, pp. 23–35.

Hicher, P.-Y., 1998. Experimental behavior of granular materials. In: Cambou, B. (Ed.), Behavior of Granular Materials. Springer Wien, New York, pp. 1–97.

Ishihara, K., Towhata, I., 1983. Cyclic Behavior of Sand during Rotation of Principal Axes. Mechanics of Granular Materials. Elsevier, pp. 55–73.

Jenkins, J.T., 1988. Volume change in small strain axisymmetric deformations of a granular material. In: Satake, M., Jenkins, J.T. (Eds.), Micromechanics of granular materials. pp. 143–152.

Jenkins, J.T., Strack, O.D.L., 1993. Mean-field inelastic behavior of random arrays of identical spheres. Mechanics of Material 16, 25–33.

Kruyt, N.P., Rothenburg, L., 2002. Micromechanical bounds for the effective elastic moduli of granular materials. International Journal of Solids and Structures 39 (2), 311–324.

Kruyt, N.P., 2003. Statics and kinematics of discrete Cosserat-type granular materials. International Journal of Solids and Structures 40, 511–534.

Li, X.S., Dafalias, Y.F., 2002. Constitutive modeling of inherently anisotropic sand behavior. Journal of Geotechnical and Geoenvironmental Engineering 128 (10), 868–880.

Liao, C.L., Chang, T.P., Young, D., Chang, C.S., 1997. Stress-strain relationship for granular materials bases on hypothesis of best fit. International Journal of Solids and Structures 34 (31–32), 4087–4100.

Liao, C.L., Chan, T.C., Suiker, A.S.J., Chang, C.S., 2000. Pressure-dependent elastic moduli of granular assemblies. International Journal for Analytical and Numerical Methods in Geomechanics 24, 265–279.

Luong, M.P., 1980. Stress–strain aspects of cohesionless soils under cyclic and transient loading. In: International Symposium on Soils under Cyclic and Transient Loading, Swansea, pp. 353–376.

Matsuoka, H., Takeda, K., 1980. A stress–strain relationship for granular materials derived from microscopic shear mechanisms. Soils and Foundation 20 (3), 45–58.

Mindlin, R.D., 1969. Microstructure in linear elasticity. Archive for Rational Mechanisms and Analysis 16, 51–78.

Nemat-Nasser, S., Zhang, J., 2002. Constitutive relations for cohesionless frictional granular material. International Journal of Plasticity 18, 531–547.

Ochai, H., Lade, P.V., 1983. Three-dimensional behavior of sand with anisotropic fabric. Journal Geotechnical Engineering, ASCE 109 (10), 1313–1328.

Oda, M., 1993. Inherent and induced anisotropy in plasticity theory of granular soils. Mechanics of Materials 16 (1–2), 35–45.

Pande, G.N., Sharma, K.G., 1982. Multi-laminate model of clays—a numerical evaluation of the influence of rotation of the principal stress axis. In: Desai, C.S., Saxena, S.K. (Eds.), Proceedings of Symposium on Implementation of Computer Procedures and Stress–Strain Laws in Geotechnical Engineering, Chicago. Acorn Press, Durham, NC, pp. 575–590.

Rothenburg, L., Selvadurai, A.P.S., 1981. Micromechanical definitions of the Cauchy stress tensor for particular media. In: Selvadurai, A.P.S. (Ed.), Mechanics of Structured Media. Amsterdam, Elsevier, pp. 469–486.

Rowe, P.W., 1962. The stress-dilatancy relations for static equilibrium of an assembly of particles in contact. Proceedings of Royal Society London A 269, 500–527.

Satake, M., 1997. A note on discrete mechanics of granular materials. In: Chang, C.S., Misra, A., Liang, R.Y., Babic, M. (Eds.), Mechanics of Deformation and Flow of Particulate Materials. ASCE, pp. 1–10.

Suiker, A.S.J., Chang, C.S., 2004. Modelling failure and deformation of an assembly of spheres with frictional contacts. Journal of Engineering Mechanics 130 (3), 283–293.

Taylor, D.W., 1948. Fundamentals of Soil Mechanics. John Wiley & Sons, New York, NY.

Wallton, K., 1987. The effective elastic moduli of a random packing of spheres. Journal of the Mechanics and Physics of Solids 35, 213–226.

Wan, R.G., Guo, P.J., 2001. Drained cyclic behavior of sand with fabric dependence. Journal of Engineering Mechanics 127 (11), 1106–1116.